ACS APPLIED MATERIALS & INTERFACES

Research Article

Cite This: ACS Appl. Mater. Interfaces XXXX, XXX, XXX−XXX

www.acsami.org

# Modifying Perovskite Films with Polyvinylpyrrolidone for Ambient-Air-Stable Highly Bendable Solar Cells

Hao Xiong,[†,‡] Giovanni DeLuca,[‡] Yichuan Rui,[§] Boxin Zhang,[†] Yaogang Li,[†] Qinghong Zhang,*[,†] Hongzhi Wang,*[,†] and Elsa Reichmanis*[,‡,∥]

[†]State Key Laboratory for Modification of Chemical Fibers and Polymer Materials, College of Materials Science and Engineering, Donghua University, Shanghai 201620, P. R. China

[‡]School of Chemical and Biomolecular Engineering, Georgia Institute of Technology, 311 Ferst Drive NW, Atlanta, Georgia 30332, United States

[§]College of Chemistry and Chemical Engineering, Shanghai University of Engineering Science, Shanghai 201620, P. R. China

[∥]School of Chemistry and Biochemistry, Georgia Institute of Technology, 901 Atlantic Drive, Atlanta, Georgia 30332, United States

Supporting Information

**ABSTRACT:** One major drawback that prevents the large-scale practical implementation of perovskites is their susceptibility to performance degradation in humid environments. Here, we achieved uniform, stable perovskite films within a polyvinylpyrrolidone (PVP) polymer frame via mild solution processing in ambient air with over 60% relative humidity. In addition to facilitating film formation, the hydrophobic PVP served to protect the perovskite grains from atmospheric moisture. Use of PVP, coupled with optimization of the deposition parameters, provided for compact, smooth, pinhole-free perovskite films that when incorporated into a photovoltaic device exhibited highly reproducible efficiencies in the range of up to 17%. In the absence of encapsulation, the devices exhibited stable performance characteristics during exposure to humid ambient air for 600 h. Furthermore, on flexible substrates, the 8 wt % PVP−perovskite samples provided for device efficiencies of ca. 15%. The devices retained ca. 73% of their efficiency after bending 1000 times with a bending radius of 0.5 cm.

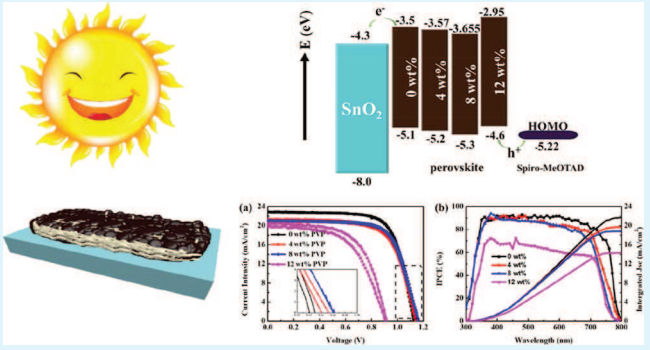


**KEYWORDS:** *perovskite solar cells, polymer doping, polyvinylpyrrolidone, long-term stability, bending stability, flexible solar cells*

## 1. INTRODUCTION

As certified by the National Renewable Energy Laboratory (NREL), the power conversion efficiency of perovskite solar cells (PSCs) has reached 22.7% when fabricated using an optimized device architecture.[1] The dramatic improvements that led to such high efficiencies were due to the excellent semiconductor properties of $ABX_3$ perovskite films, such as a high absorption coefficient in the visible region, ambipolar charge transport, and long carrier lifetime.[2−5] The benefits of perovskites are also reflected in their ease of synthesis that has enabled fabrication of high efficiency devices using various solution deposition techniques, such as spin-coating,[6] doctor-blade coating,[7] slot-die coating,[8] or ink-jet printing.[9] Even though solvent[6] and interfacial engineering[10] have led to more homogeneous and relatively defect-free perovskite films, a number of key issues remain. In particular, if PSCs are to be technologically and commercially viable, challenges that must be overcome include not only the inherent toxicity of the material due to the presence of lead, but more importantly, limited device lifetimes associated with susceptibility to ambient air and possible ion migration within the crystal lattice. Thus, for PSCs to be able to generate electricity continuously, long-term stability is a necessary prerequisite, and further, the crystal structure must be stabilized in order to obtain high efficiency devices with steady output power.[11]

Efforts to address perovskite stability include approaches such as interface modification,[12] dopants,[13] component selection,[14] and encapsulation,[15] among others. For instance, Grätzel and co-workers modified the surface of $MAPbI_3$ by spin-coating its precursor solution in the presence of butylphosphonic acid 4-ammonium chloride,[16] while others used a self-assembled hydrophobic fluoroalkylsilane coating on the surface of the perovskite films.[17] Very recently, it was reported that the addition of a polymer into the precursor solution, in a one-step deposition process, can tune perovskite morphology, thereby enhancing device stability in air. Examples of polymers that have been explored include polyethylene glycol,[18] phenethylamine,[19] polyurethane,[20] and

Received: March 15, 2018
Accepted: August 28, 2018
Published: August 28, 2018






DOI: 10.1021/acsami.8b04236
ACS Appl. Mater. Interfaces XXXX, XXX, XXX−XXX

so forth. However, incorporation of these polymers into the film had a negative impact on the $MAPbI_3$ perovskite film morphology because of steric effects.

Polyvinylpyrrolidone (PVP) is an alternative polymer that has been investigated in efforts to stabilize the active layer; however, the resultant perovskite films continued to have an unacceptably high number of defects.[21−23] PVP is an attractive additive because of its strong polar carbon-oxygen double bond, which is expected to interact with the perovskite precursor components and thereby stabilize the perovskite crystal structure. In addition, there are nontrivial challenges for flexible solar cells, such as interfacial contact, deposition technologies, module manufacture, and long-term and bending stability.[24] Among these challenges, bending stability is of prime importance.

Here, we demonstrate how commercial PVP, coupled with optimization of the deposition parameters, provides for defect-free perovskite films. PVP K-30 ($M_w$ = 40 000 g/mol; *K*-value of viscosity for a 1% solution ∼30) was directly introduced into the perovskite precursor solution, and through optimization of the perovskite precursor to additive ratio, was shown to facilitate formation of highly compact and uniform films, which in a device configuration exhibited efficiencies as high as 17%. The PVP−perovskite system displayed excellent stability upon storage in ambient air (relative humidity ≥ 60%) and further, was shown to provide a platform for flexible perovskite device fabrication.

## 2. EXPERIMENTAL SECTION

**2.1. Materials and Reagents.** All materials were purchased from Sinopharm Chemical Reagent Co., Ltd. and used as received, with the exception of the following: $CH(NH_2)_2I$ (FAI), $CH_3NH_3Br$ (MABr), and Spiro-MeOTAD (2,2′,7,7′-tetrakis [*N*,*N*-di(4-methoxyphenyl) amine)-9,9′-spirobifluorene, purity ≥ 99.5%) were purchased from Xi'an Polymer Light Technology Corp. Fluorine-doped tin oxide (FTO)-coated glass (14 Ω $sq^{-1}$) and indium tin oxide (ITO)-coated PET (polyethylene terephthalate) (7 Ω $sq^{-1}$) were purchased from Nippon Sheet Glass Co., Ltd. PVP ($M_w$ = 40 000 g/mol) was purchased from Sigma-Aldrich.

**2.2. Fabrication of the Perovskite Device.** FTO conductive glass was washed through sequential ultrasonic treatment in detergent, acetone, ethanol, and deionized water, and was then treated in an $O_2$ plasma for 30 min (DT-01, Suzhou Omega Machinery Electronic Technology Co., Ltd.). Low-temperature $SnO_2$ electron transport layers (ETLs) were prepared according to the method described by Chattopadhyay.[25] $SnCl_2{\cdot}2H_2O$ (22.56 mg) was dissolved in 10 mL of isopropyl alcohol, and the resulting solution was stirred at reflux temperature (70 °C) for 1 h and then aged for 6 h to form the sol. A volume of 50 μL of nanoparticle $SnO_2$ sol was spin-coated onto either an FTO glass or ITO/PET substrate and then sintered on a hotplate at 90 °C for 3 h.

$PbI_2$ (507 mg, 1.1 mmol), $PbBr_2$ (73.4 mg, 0.2 mmol), FAI (172 mg, 1.0 mmol), and $CH_3NH_3Br$ (22.4 mg, 0.2 mmol) with 0−12 wt % PVP were added to 1.0 mL of dimethylformamide and dimethylsulfoxide (4:1, v/v), and the resulting mixture was stirred at 80 °C until all components were dissolved. The resulting hybrid perovskite precursor solution was spin-coated onto $SnO_2$/FTO or $SnO_2$/ITO substrates at 3000 rpm for 30 s using a one-step method. During spin-coating, the samples were washed with toluene, a nonpolar solvent. The perovskite films were then annealed at 110 °C for 10 min on a hotplate while covered by a Petri dish to further remove residual solvents. A Spiro-OMeTAD solution (25 μL) was then spin-coated onto the as-prepared perovskite film at 4000 rpm for 30 s. All operations were carried out in ambient air without controlling relative humidity.[26] Finally, the devices were coated with an 80 nm gold electrode by evaporation through an aperture mask in a vacuum chamber. The active area of the perovskite device was 0.16 $cm^2$.

**2.3. Characterization.** The perovskite films were characterized by X-ray diffraction (XRD) (model D/max 2550V, Rigaku Co. Tokyo, Japan) by using Cu K$\alpha$ ($\lambda$ = 1.5406 Å) radiation. The morphology of the resultant perovskite film was observed by using field-emission scanning electron microscopy (FESEM, model S-4800, Hitachi, Japan). Tapping mode atomic force microscopy (AFM) imaging was carried out using a Multimode NanoScope IV system (Veeco, Santa Barbara, CA) at a scanning range and speed of 2 μm and 3.001 Hz, respectively. Steady-state photoluminescence (PL) spectra were acquired with a FLS920 transient optical spectrometer (Edinburgh Instruments, UK). Ultraviolet photoelectron spectroscopy characterization of the PVP−perovskite film was performed using a monochromatic He I light source (21.2 eV) and a VG Scienta R4000 analyzer. The photocurrent density−voltage ($J$−$V$) curves of the PSCs were acquired using a Keithley 2400 Source Measuring Unit. A solar simulator (model 96160 Newport Co., USA) equipped with a 300 W xenon lamp was used as a light source, where the light intensity was adjusted using an NREL-calibrated Si solar cell with a KG-1 filter for approximating the AM 1.5G one sun light intensity. The cell performance parameters, including short-circuit current density ($J_{sc}$), open-circuit voltage ($V_{oc}$), fill factor (FF = $P_{max}/(J_{sc}V_{oc})$), and photoelectron conversion efficiency ($h$ (%) = $J_{sc} \times V_{oc} \times$ FF/total incident energy × 100), were measured and calculated from the $J$−$V$ characteristics. The incident-photon-to-current conversion efficiency (IPCE) spectra were measured as a function of wavelength from 300 to 800 nm using a specially designed IPCE system (Newport Co., USA). Measurement and storage of the devices were performed in ambient conditions and without encapsulation.

## 3. RESULTS AND DISCUSSION

**3.1. PVP−Perovskite Film Formation.** While a one-step perovskite deposition method generally leads to films comprising large, cuboidal grains,[27] upon storage in humid (relative humidity greater than 60%) environments, the perovskite layers decompose rapidly. It was postulated that water catalyzes the decomposition of perovskites through the reversible reactions shown below[28]

$$[CH_3NH_3^+PbI_3]_n + H_2O \rightleftarrows [(CH_3NH_3^+)_{n-1}(PbI_3)_n][H_3O^+] + CH_3NH_2 \quad (1)$$

$$[(CH_3NH_3^+)_{n-1}(PbI_3)_n][H_3O^+] \leftrightarrows HI + PbI_2 + [(CH_3NH_3^+)(PbI_3)_{n-1} + H_2O] \quad (2)$$

Here, we describe the preparation of perovskite films with not only enhanced stability, but also flexibility, under ambient conditions using PVP as an additive, coupled with optimization of the deposition parameters. PVP was selected because of its polar characteristics that derive from the carbon−oxygen double bond (carbonyl group: C═O) present on each monomer unit. The C═O group was expected to interact with other polar species present in the perovskite precursor solution through hydrogen bonding, thereby facilitating incorporation of the polymer into the active material matrix during film deposition. Mechanistically, the long chain PVP was expected to form a framework around the perovskite crystals, thus creating a barrier to moisture penetration into the inorganic lattice. In addition, it was anticipated that incorporation of the flexible polymer might allow some latitude in bending devices fabricated on plastic substrates, thereby maintaining performance.

As evidenced by the FESEM surface and cross-sectional images (Figure 1a−d,i−l, respectively), perovskite morphology


DOI: 10.1021/acsami.8b04236
ACS Appl. Mater. Interfaces XXXX, XXX, XXX−XXX

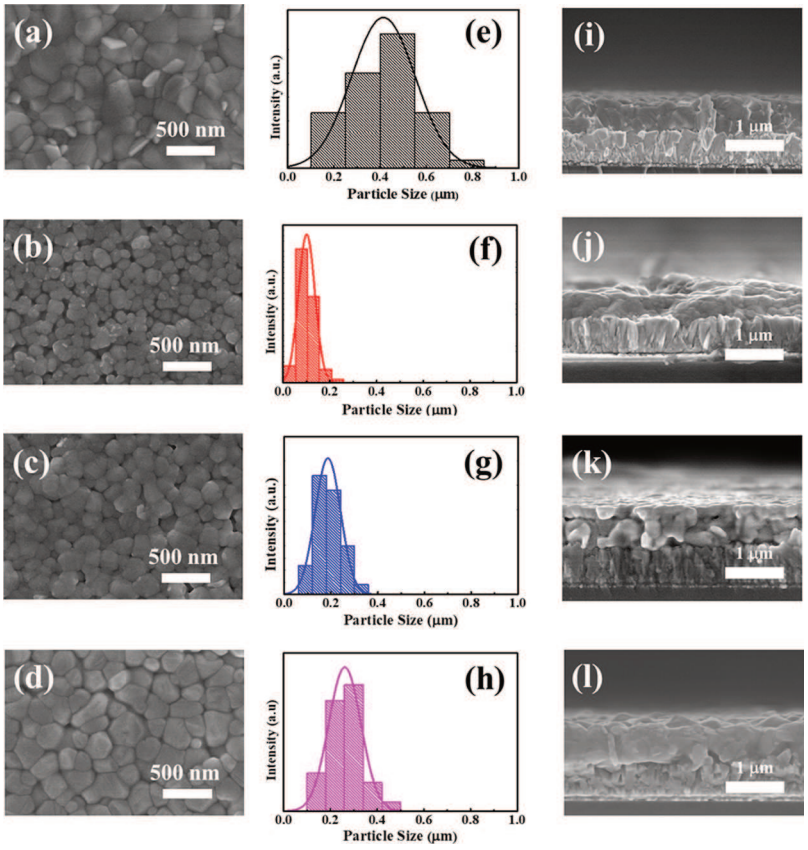


**Figure 1.** Surface and cross-sectional FESEM image of perovskite films without PVP (a,i) and with PVP at 4 (b,j), 8 (c,k), and 12 wt % (d,l) concentrations. Particle size and distribution for corresponding images (e–h).

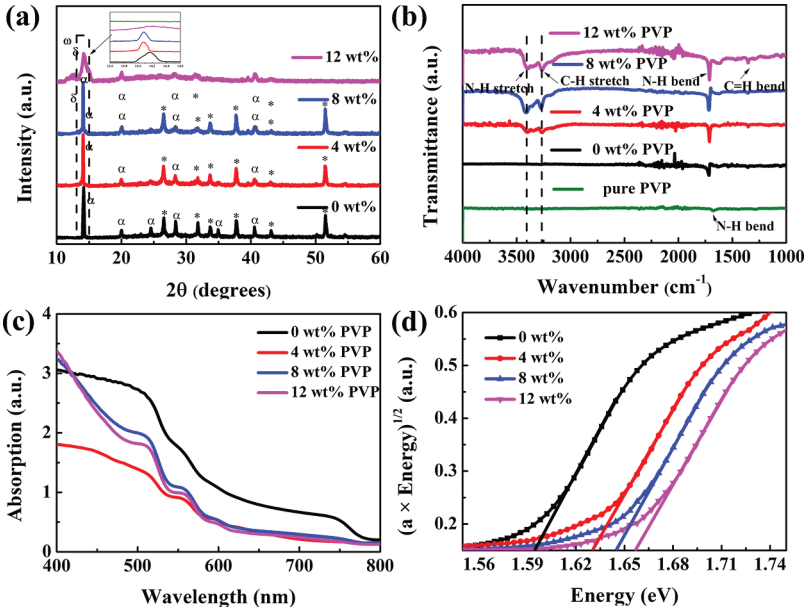


**Figure 2.** (a) XRD patterns of 0 wt % (black), 4 wt % (red), 8 wt % (blue), and 12 wt % (magenta) PVP–perovskite films. The diffraction peaks originating from the perovskite phase, nonperovskite phase, unreacted $PbI_2$ and the FTO substrate are marked by $\alpha$, $\delta$, $\omega$, and * respectively. (b) FT-IR spectra of 0 wt % (black), 4 wt % (red), 8 wt % (blue), and 12 wt % (magenta) PVP–perovskite films, and pure PVP (green); (c) UV–vis absorbance data of 0 wt % (black), 4 wt % (red), 8 wt % (blue), and 12 wt % (magenta) PVP–perovskite films; and (d) Tauc plots of 0 wt % (black), 4 wt % (red), 8 wt % (blue), and 12 wt % (magenta) PVP–perovskite films.

changed dramatically upon incorporation of PVP, and notably, the PVP-modified layers appeared more uniform and homogeneous. As presented in Figure 1e–h, the particle/grain size changed when PVP was added to the precursor solution; for 0, 4, 8, and 12 wt % PVP–perovskite films, the grain sizes were ca. 400, 100, 210, and 350 nm, respectively. In



DOI: 10.1021/acsami.8b04236
ACS Appl. Mater. Interfaces XXXX, XXX, XXX–XXX

addition, in the presence of PVP, the perovskite films exhibited a narrower particle size distribution. While in all cases, inclusion of PVP afforded more homogeneous structures, when the concentration of PVP exceeded 12 wt %, the film appeared to develop large voids between individual perovskite grains. This is attributed to inductive effects[29] and the space location-obstruct effect[30] associated with PVP leading to transformation of the perovskite crystals (vide infra). AFM analysis (Figure S1a–d, Supporting Information) provided insight into the surface roughness of the as-prepared films (Sq, root mean square height). Whereas the parent perovskite presented a Sq value of 19.34 nm (Figure S1a), that for 4.0 wt % PVP (Figure S1b) was only 7.96 nm, meaning that the surface was much smoother. For comparison, Sq for 8 and 12 wt % PVP–perovskite was 14.32 nm (Figure S1c) and 17.39 nm (Figure S1d), respectively. The AFM results were consistent with SEM observations.

From examination of the characteristic XRD patterns presented in Figure 2a, 0, 4, and 8 wt % PVP–perovskite grains on FTO glass were well-crystallized, presenting signature peaks at $2\theta$ = 20.08° (200), 28.35° (220), and 40.81° (400). However, several different peaks were observed in the diffraction patterns owing to the varying PVP content. With the increasing PVP concentration, the characteristic $2\theta$ perovskite peak at 14.39° underwent a shift to a slightly lower value, as seen in the upper inset. This shift is indicative of residual stress between PVP and the perovskite crystals, which is a phenomenon found in other materials.[31] At lower PVP concentrations, this stress did not significantly influence the overall film morphology. However, for PVP content above 12%, diffraction peaks attributed to residual $PbI_2$ and stress-induced damage to the crystal structure were observed at $2\theta \approx$ 12.6° (001). Conceivably, the small feature observed at 12.6° originates from the nonperovskite phase of $FAPbI_3$ that begins to form at higher concentrations of PVP. The XRD analysis is consistent with the morphologies identified by SEM (Figure 1): note the lighter, roughened edges of the perovskite grains in Figure 1d.

Fourier transform infrared (FT-IR) spectroscopy was used to investigate the presence of chemical interactions between PVP and the perovskite. Spectra within the range of 4000–1000 $cm^{-1}$ for pure PVP, pristine perovskites, and PVP–perovskite films with varying concentrations of PVP are presented in Figure 2b. The higher polymer concentration sample was selected for FTIR analysis to enable identification of interactions and band shifts. The main spectral features to be considered in the pure PVP film are the tertiary amine group deformation modes at 1458 $cm^{-1}$ and the carbonyl group vibration at 1676 $cm^{-1}$.[32] The C–N bending vibration appears at 1716 $cm^{-1}$ in pristine perovskites; however, in the presence of PVP, the C–N band shifts to lower wavenumbers as the PVP concentration is increased. This observed shift may derive from interactions between perovskite C–N and PVP C=O groups. While peaks associated with C–N and N–H stretching are not obvious in the pristine perovskite film; the PVP C–H and N–H vibrational modes appear as intense bands at 3500–3000 $cm^{-1}$ in PVP-doped films.

UV–vis spectral analysis (Figure 2c) demonstrated that the incorporation of PVP into the perovskite layer led to a slight decrease in the absorption of visible light, where the parent perovskite exhibited the highest absorbance. The band gap was calculated by applying Kubelka–Munk (K–M) analysis to the measured diffuse absorption spectra as follows[33]

$$(\alpha h\nu)^2 = C(h\nu - E_g) \quad (3)$$

where $\alpha$ represents the absorption coefficient, $h$ represents Planck's constant, $\nu$ is the frequency of light, $E_g$ is the band gap of the material, and $C$ is the proportionality constant—not related to $E_g$. The Tauc plot presented in Figure 2d was used to determine the perovskite band gap as a function of the PVP concentration. While the pristine perovskite band gap was calculated to be 1.60 eV, incorporation of up to 12 wt % PVP led to a gradual increase in band gap to 1.65 eV (Table 1). This change is attributed to the $Pb^{2+}$ 4f core-level peak shift, which dominates the perovskite band gap.[34]

**Table 1. Band gap Values Calculated from UV–Vis and Ultraviolet Photoelectron Spectroscopy Data**

| PVP concentration (wt %) | band gap (eV) | valence band (eV) | conduction band (eV) |
|---|---|---|---|
| 0 | 1.60 | −5.1 | −3.5 |
| 4 | 1.63 | −5.2 | −3.57 |
| 8 | 1.645 | −5.3 | −3.655 |
| 12 | 1.65 | −4.6 | −2.95 |

Ultraviolet photoelectron spectroscopy (UPS) was used to evaluate the effect of PVP on perovskite electronic properties.[35] Notably, incorporation of PVP led to a significant decrease in energy of the valence band (EVB) from −5.1 to −5.3 eV, as measured by UPS, using He(I) emission ($h\nu$ = 21.2 eV) as the light source (Figure S2). The VB edge energy EVB values, with reference to the vacuum level, were calculated to be −5.1 eV for the parent, and −5.2, −5.3, and −4.6 eV for the 4, 8, and 12 wt % PVP–perovskites, respectively. The conduction band edge energies (ECBs) were then determined from the $E_g$ and EVB values; ECB for the parent was −3.5 eV, a value that is slightly deeper than that of the 4 and 8 wt % PVP–perovskite samples (−3.6, −3.7 eV). The incorporation of 12 wt % PVP afforded a material having an ECB value of −2.95 eV, pointing to the existence of a nonperovskite phase. In principle, the deeper perovskite conduction band would be expected to enhance charge transfer from the perovskite to the ETL.[36]

X-ray photoelectron spectroscopy (XPS) analysis was used to further investigate the changes in binding energy of the perovskite core-level peaks in the presence and absence of additives. The survey spectra of perovskite prepared with the varying PVP concentration are presented in Figure S3. All of the samples were prepared on silicon substrates, and all exhibit nearly the same XPS peaks and intensities, indicating that the components of all films are the same. The iodine, oxygen, nitrogen, carbon, lead, and bromide atom binding energies are shown in Figure 3a–f. The spin–orbit split components of I $3d_{3/2}$ and I $3d_{5/2}$ are shifted slightly to lower energy (Figure 3a). The peak height of the I 3d peaks (arising from $PbI_6$ octahedra) decreases slightly with increasing PVP content. Abnormal deviations can also be observed in the split components of O 1s, N 1s, C 1s, Pb 4f, and Br 3d (Figure 3b–f), which, consistent with XRD analysis, supports the premise that the $PbI_6$ octahedra were disrupted by PVP chains.

Even more remarkably, the spin–orbit split components of pristine perovskites show low strengths at 533.3 and 532 eV for O $1s_{2/2}$ and O $1s_{1/2}$, respectively. The peak at 533.3 eV corresponds to adsorbed molecular water.[37] With PVP doping, the 533.3 eV peak is absent, suggesting that PVP serves as a


DOI: 10.1021/acsami.8b04236
ACS Appl. Mater. Interfaces XXXX, XXX, XXX–XXX

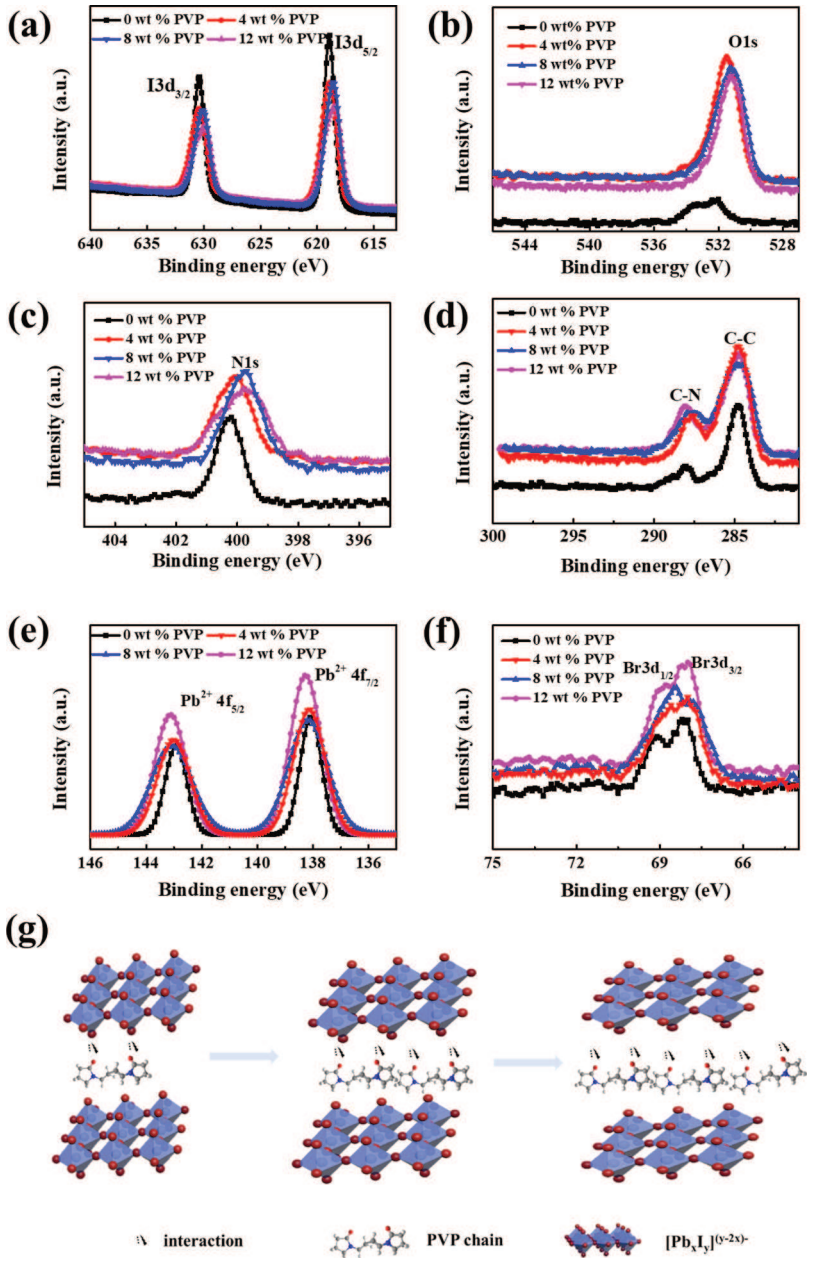


**Figure 3.** Core-level XPS spectra for 0 wt % (black), 4 wt % (red), 8 wt % (blue), and 12 wt % (magenta) PVP–perovskite films: (a) I 3d, (b) O 1s, (c) N 1s, (d) C 1s, (e) Pb 4f, and (f) Br 3d. (g) Schematic representation of the variation of perovskite crystals with the increasing PVP concentration.

barrier to protect the perovskite film from adventitious water. Simultaneously, the C═O group peak near 532 eV increased in intensity. Slightly shifted peaks were observed in the doped perovskite, which may derive from hydrogen bonding interactions between PVP and perovskites.[32] The experimental Pb 4f signal is presented in Figure 3e; spin–orbit splitting between the Pb $4f_{7/2}$ and Pb $4f_{5/2}$ lines of pristine perovskites appeared at 138.1 and 143 eV, respectively. However, the $Pb^{2+}$ lines of the doped perovskite shifted to higher binding energies. The shift of the Pb 4f levels can be attributed to decreased electron cloud overlap between the lead and iodide atoms, which may help account for the observed slight increase in band gap (vide infra).[34]

To further explain the phenomenon, a schematic representation of the interactions between perovskite crystals and the PVP long chain is presented in Figure 3g. With the increased PVP concentration, the $PbI_6$ octahedra become stretched. Up to a PVP concentration of about 8 wt %, the $[Pb_3I_8]^{2-}$ octahedra are able to tolerate the distortions; however, upon continued increased PVP content, the $[Pb_3I_8]^{2-}$ crystal lattice rearranged to form octahedral $[PbI_6]^{4-}$, resulting in the formation of a nonperovskite phase. The presence of $[PbI_6]^{4-}$ also impacts the absorption edge of the samples, as discussed below.[38]

PL spectroscopy provided insight into the charge carrier extraction properties of solar cells fabricated from pure and PVP-containing perovskite active materials. An obvious change in PL intensity was observed for PVP–perovskite films versus the parent (Figure S4a). Specifically, the higher PL intensity for the 4 and 8 wt % PVP–perovskite samples suggests that


DOI: 10.1021/acsami.8b04236
ACS Appl. Mater. Interfaces XXXX, XXX, XXX–XXX

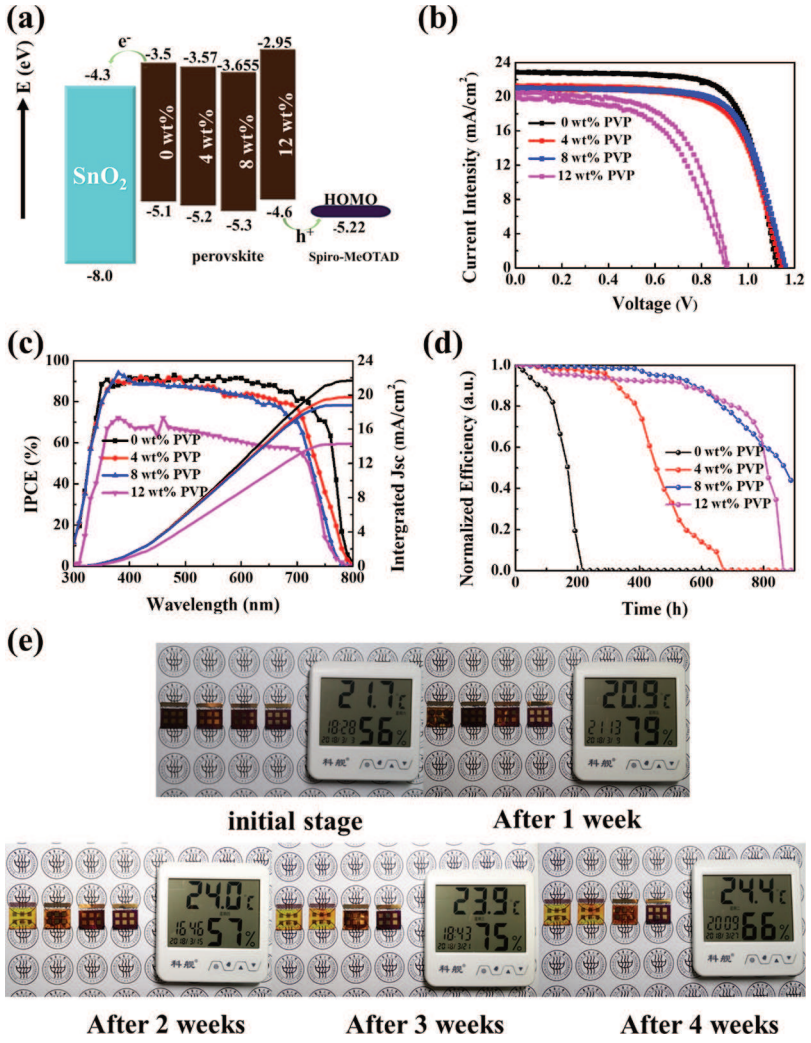


**Figure 4.** (a) Schematic energy-level diagrams of the $SnO_2$ nanoparticles, 0, 4, 8, and 12 wt % PVP-doped perovskite and Spiro-MeOTAD; (b) $J-V$ curves of the typical devices under AM 1.5G illumination. (c) Corresponding EQE responses (left axis) and integrated current densities (right axis) of the devices containing the perovskite films with and without PVP. (d) Normalized efficiency as a factor of time; (e) photograph of perovskite solar cell stability with varying concentrations of PVP in ambient conditions. From left to right, 0, 4, 8, and 12 wt % PVP−perovskite devices.

these films possess fewer defects. The 12 wt % counterpart exhibited a decrease in PL intensity, suggesting an increase in defect density as PVP content increased above 8 wt %. Time-resolved PL (TRPL) spectra demonstrated that the presence of PVP also impacts PL lifetime, where the 8 wt % sample exhibited a notably longer lifetime than any of the alternatives (Figure S4b). Combined, the PL and TRPL results suggest that at low levels (below about 8 wt %), the incorporation of PVP into the perovskite crystal structure facilitates formation of more uniform films having fewer defects.

**3.2. Device Fabrication and Characterization.** Perovskite-based solar cells were fabricated using optimized processing conditions under ambient conditions. The device architecture comprised either glass/FTO/compact $SnO_2$/perovskite/Spiro-OMeTAD/Au, or PET/ITO/compact $SnO_2$/perovskite/Spiro-OMeTAD/Au. Figure 4a presents a sketch of the band alignment scheme for a photovoltaic device fabricated using the hybrid active material. To avoid hysteresis, which is in part a function of the quality of the interface between the perovskite and ETL, $SnO_2$ nanoparticles were used as the ETL.[39−41] Because the $SnO_2$ nanoparticle deposition temperature is typically ca. 200 °C, a sol−gel method was developed to enable process temperatures below 185 °C in order to fabricate an $SnO_2$ ETL that is also suitable for plastic substrates.

Figure 4b presents the current−voltage curves of the pristine and PVP containing PSCs fabricated on glass/FTO substrates, and the data are tabulated in Table S1. Furthermore, statistical data regarding the photovoltaic parameters are plotted in Figure S5. Cells fabricated from the 0, 4, and 8 wt % PVP−perovskites exhibited little hysteresis, while hysteresis was significant for the 12 wt % PVP−perovskite cells. The parent PSCs exhibited efficiencies of 18.42 and 18.38% under reverse and forward scans, respectively, with the corresponding $V_{oc}$ of 1.127 and 1.124 V, $J_{sc}$ of 22.8 and 22.9 mA/cm$^2$, and FF of 71.43 and 71.7%. Upon incorporation of 4 wt % PVP, device efficiency in the forward and reverse directions decreased slightly to 16.7 and 16.41%, while the corresponding $V_{oc}$, $J_{sc}$, and FF values were 1.15 and 1.14 V, 21.2 and 20.9 mA/cm$^2$, and 68.73 and 68.07%, respectively. The 8 wt % PVP−perovskite device exhibited negligible hysteresis, with an efficiency of 17.04 and 17.06%, a $V_{oc}$ of 1.16 and 1.162 V, $J_{sc}$ of 21 and 21.05 mA/cm$^2$, and FF of 70.01 and 69.69% under reverse and forward scan, respectively. The excellent perform-


DOI: 10.1021/acsami.8b04236
ACS Appl. Mater. Interfaces XXXX, XXX, XXX−XXX

ance can be ascribed to the matched band gap and defect-free crystals, which is in accord with the structural analysis mentioned above. The improved performance of the 8 wt % PVP devices versus their 4 wt % alternatives is likely due to many factors which can affect FF. Among these are series resistance and parallel resistance, both of which are related with perovskite morphology and defects. While the 4% PVP sample has lower roughness, the number of grain boundaries is larger as a result of the smaller perovskite grain size. Conceivably, PVP may also more effectively passivate defects within perovskite grains with the increasing concentration. Further, $V_{oc}$ increased upon incorporation of PVP. Thus, as a result of many factors, for the 8 wt % PVP samples, the FF increased slightly.

As expected from the materials characterization results, devices fabricated from 12 wt % PVP–perovskite films exhibited a significant decline in performance, namely, a PCE of only 11.31% under the reverse scan and 10.18% under the forward scan. $V_{oc}$, $J_{sc}$, and FF were similarly negatively affected. Presumably, the low FF of 56.84 obtained for the 12 wt % PVP containing cells is due to the rough perovskite morphology. It is widely believed that the key parameter associated with perovskite device performance is the FF, which may be negatively affected by carrier recombination at the interface between the perovskite and the electron/hole transport layers due to perovskite crystal degradation.[42]

Figure 4c presents the IPCE data for the devices studied here. The wavelength at which the IPCE curves experience a rapid rise is consistent with the absorption edge data discussed above: for the parent perovskite, the increase appeared at around 780 nm, while for cells fabricated with 4, 8, and 12 wt % PVP–perovskite, IPCE began to increase at about 770, 760, and 750 nm, respectively. Between 450 and 700 nm, the absorption profile of devices based on pristine perovskites was higher than those for the doped materials, which may derive from the perovskite grain size.[43] Between 350 and 450 nm, the absorption of the 12 wt % device decreased sharply, likely because of incomplete perovskite grain formation.[44]

Data associated with the moisture sensitivity of the perovskite devices investigated here are presented in Figure 4d,e. The parent perovskite underwent a steady decrease in efficiency from 18 to ~1% within 200 h. Notably, the devices fabricated with PVP modification exhibited enhanced resistance to moisture present in the ambient conditions. Incorporation of 8 wt % PVP into the perovskite layer allowed fabrication of devices that retained 80% of their original efficiency for over 600 h under ambient conditions with 60% relative humidity. Although the initial efficiency of the 12 wt % PVP–perovskite devices was lower than the other analogs, the normalized efficiency appeared more stable in a humid environment, presumably directly related to protection of the perovskite by PVP. To furtherly identify the lower degradation rate in unencapsulated doped perovskite devices, XRD spectra of the nondoped perovskite film (a), 4 wt % PVP (b), 8 wt % PVP, and 12 wt % PVP doped perovskite films were evaluated as presented in Figure S6. The fraction of the perovskite phase was determined from the area of its main peaks at (110) and (220) planes,[45] which confirmed that degradation of the nondoped device is mainly attributed to rapid, humidity-induced decomposition of the perovskite film in air. In contrast, the PVP-doped perovskite films exhibited a much lower degree of decomposition.

**3.3. Flexibility and Bendability Testing.** Given the superior performance of the perovskite comprising 8 wt % PVP, that composition was selected to explore the impact of PVP incorporation into the perovskite lattice on active layer flexibility. Top-view SEM images of the parent and PVP–perovskite films fabricated on an ITO/PET substrate and subjected to mechanical bending (200 times with bending radius of 0.5 cm) are presented in Figure 5. As expected, the

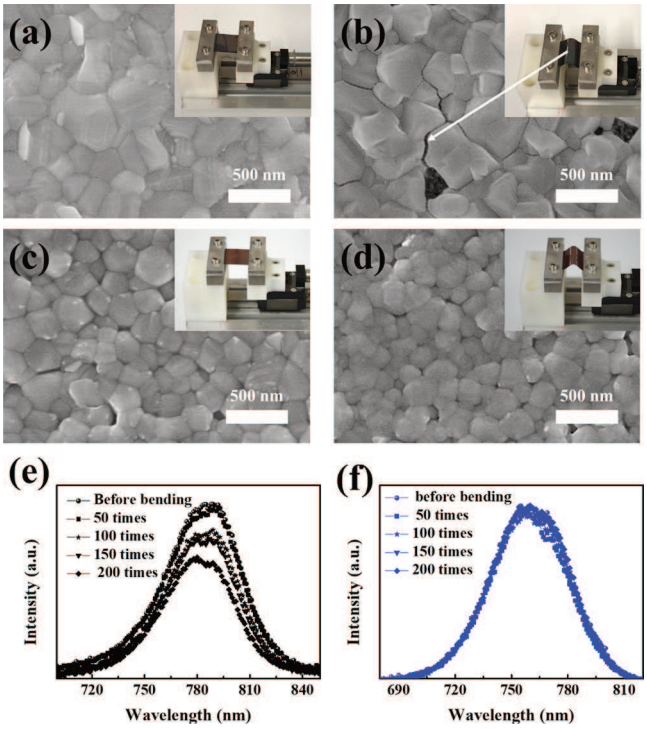


**Figure 5.** (a–d) Top-view SEM images of (a,b) 0 wt % PVP and (c,d) 8wt % PVP–perovskite grown on PET/ITO before and after 200 bending times with a bending radius of 0.5 cm; the inset shows a photograph of the bending tests; (e,f) steady-state PL spectra of the corresponding pristine and PVP containing perovskite films.

parent perovskite film (Figure 5a) exhibited evidence of fracturing at the grain boundaries upon bending 200 times (Figure 5b). In contrast, films fabricated with 8 wt % PVP (Figure 5c) displayed a uniform morphology that did not appear compromised (Figure 5d). Conceivably, the incorporation of PVP into the crystalline film forms a polymer network, effectively improving the mechanical properties of the active layer.[20] Furthermore, steady-state PL spectra (Figure 5e,f) of the corresponding perovskite films on PET/ITO before and after bending 200 times were also analyzed. The PL intensity of the 8 wt % PVP–perovskite film (Figure 5f) prepared on PET/ITO was similar to that of pristine material (Figure 5e) prior to mechanical bending. After bending 200 times, the PVP–perovskite maintained its PL intensity, while that of the pristine film noticeably decreased. These results strongly suggest that the incorporation of PVP serves to reduce surface defects and importantly, for envisioned flexible PSC applications, instills the films with improved mechanical performance attributes.

To further investigate the impact of PVP on the performance of the perovskite films under bending-induced stress, PET/ITO/$SnO_2$/perovskite/Spiro-MeOTAD/Au devices were fabricated and subjected to multiple bending cycles


DOI: 10.1021/acsami.8b04236
ACS Appl. Mater. Interfaces XXXX, XXX, XXX–XXX

where the curvature was 5 mm for each cycle, as shown in Figure 6. Before bending, the PCE of PET/ITO-based devices

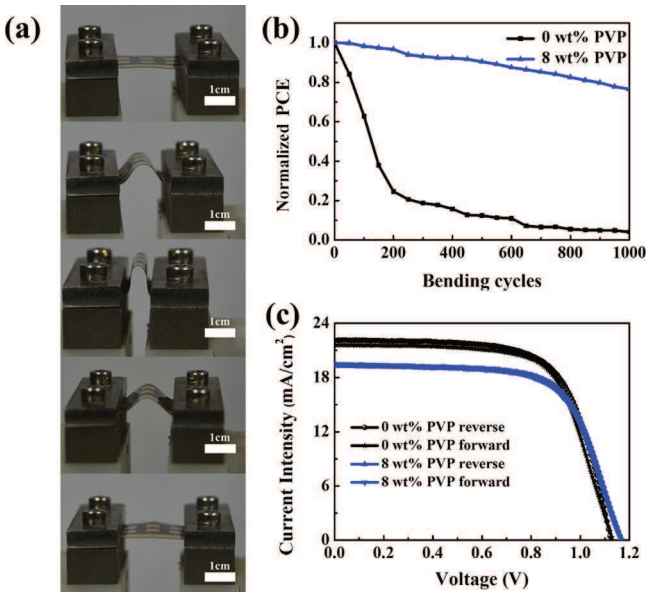


**Figure 6.** (a) Photograph of the bending tests for flexible devices; (b) $J-V$ curves of 0 and 8 wt % PVP−perovskite flexible devices under AM 1.5G illumination at the initial stage; (c) mechanical stability of corresponding flexible devices.

fabricated with perovskite active layers having 0 and 8 wt % PVP was 16.77 and 15.3%, with corresponding $V_{oc}$ of 1.124 and 1.169 V, $J_{sc}$ of 22.13 and 19.48 mA/cm$^2$, and FF of 67.41 and 67.67%, respectively. After 1000 bending cycles, the device fabricated using 8 wt % PVP−perovskite retained more than 70% of its original efficiency, whereas the pristine device exhibited less than 10% retention of its PCE. Complete data (before and after bending 1000 times) associated with flexible solar cell performance is presented in Table S2. Note that the $V_{oc}$ slightly decreased in both cases, while short-circuit current decreased only slightly for the PVP containing active layer versus the sharp decline observed when solar cells fabricated with pristine perovskites were bent 1000 times. Presumably, the decreased values of $V_{oc}$ and $J_{sc}$ are due to the inorganic $SnO_2$ film which is known to have poor flexibility.[46] The device results demonstrate that intercalation of PVP into the perovskite lattice can positively impact the mechanical properties of the hybrid active layer, allowing for the design and development of flexible devices.

## 4. CONCLUSIONS

In summary, PVP was introduced into a perovskite precursor solution and effectively integrated into the resultant perovskite films. Incorporation of the polymer was shown to both protect the active material against degradation under humid ambient conditions and impart mechanical flexibility. Mechanistically, it is believed that PVP interacts with the perovskite via hydrogen bonding facilitated by the presence C═O bonds along the polymer chain. The results demonstrated that with an increased proportion of PVP, the perovskite crystal size increased, while XRD peaks shifted slightly, confirming the presence of chemical/physical interactions between the two components. PVP−perovskite-based solar cells comprising 8 wt % polymer additives exhibited a power conversion efficiency of 17%. The device efficiency remained above 15% for a duration of more than 600 h under ambient conditions (>60% humidity). Moreover, incorporation of PVP into the active layer facilitated fabrication of flexible solar cells, with an efficiency of ca. 15%, whereby the efficiencies were stable over several bending cycles. The results presented here demonstrate that polymer additives, such as PVP, that can effectively interact with the inorganic perovskite crystal can lead to environmentally stable and flexible PSCs. Modification of the perovskite through incorporation of a polymer additive is expected to enable the low-cost, large-scale fabrication of robust perovskite-based solar cells.

## ■ ASSOCIATED CONTENT

### Supporting Information

The Supporting Information is available free of charge on the ACS Publications website at DOI: 10.1021/acsami.8b04236.

AFM images of 0 wt % (a), 4 wt % PVP (b), 8 wt % (c), and 12 wt % (d) PVP−perovskite films; valence band spectra of perovskite films with 0 (a), 4 (b), 8 (c), and 12 wt % (d) PVP on silica wafer; survey XPS spectra of 0 wt % (black), 4 wt % (red), 8 wt % (blue), and 12 wt % (magenta) PVP-perovskite samples; photoluminescence of 0 wt % (black), 4 wt % (red), 8 wt % (blue), and 12 wt % (magenta) PVP−perovskite samples on the glass and (b) time-resolved photoluminescence (TRPL) data for 0 wt % (black), 4 wt % (red), 8 wt % (blue), and 12 wt % (magenta) PVP−perovskite samples; statistical data: 0 wt % (black), 4 wt % (red), 8 wt % (blue), and 12 wt % (magenta) for (a) $V_{oc}$, (b) $J_{sc}$, (c) FF, and (d) PCE; and XRD spectra of the nondoped perovskite film (PDF)

## ■ AUTHOR INFORMATION

### Corresponding Authors

*E-mail: zhangqh@dhu.edu.cn. Phone: +86-21-67792943. Fax: +86-21-67792855 (Q.Z.).
*E-mail: wanghz@dhu.edu.cn (H.W.).
*E-mail: elsa.reichmanis@chbe.gatech.edu (E.R.).

### ORCID

Giovanni DeLuca: 0000-0002-3456-1020
Hongzhi Wang: 0000-0002-5469-2327
Elsa Reichmanis: 0000-0002-8205-8016

### Notes

The authors declare no competing financial interest.

## ■ ACKNOWLEDGMENTS

We gratefully acknowledge the financial support by the Program for Professor of Special Appointment (Eastern Scholar) at Shanghai Institutions of Higher Learning, the Major Program of the National Natural Science Foundation of China (51590902). Program of Shanghai Academic Research Leader (16XD1400100), Science and Technology Commission of Shanghai Municipality (16JC1400700), Innovation Program of Shanghai Municipal Education Commission (2017-01-07-00-03-E00055), and the Program of Introducing Talents of Discipline to Universities (no. 111-2-04) are also acknowledged. We also appreciate support from the National Science Foundation, NSF EAGER 1665279. H.X. thanks the China Scholarship Council and the Fundamental Research Funds for the Central Universities (CUSF-DH-D-2017038).


DOI: 10.1021/acsami.8b04236
ACS Appl. Mater. Interfaces XXXX, XXX, XXX−XXX

G.D. is grateful for support from the NSF EAPSI program, OISE 1613514; E.R. thanks the Georgia Institute of Technology for support and additionally appreciates support from the Brook Byers Institute for Sustainable Systems at Georgia Tech.

## REFERENCES

(1) Yang, W. S.; Park, B.-W.; Jung, E. H.; Jeon, N. J.; Kim, Y. C.; Lee, D. U.; Shin, S. S.; Seo, J.; Kim, E. K.; Noh, J. H.; Seok, S. I. Iodide management in formamidinium-lead-halide-based perovskite layers for efficient solar cells. *Science* **2017**, *356*, 1376−1379.

(2) Wolf, S. D.; Holovsky, J.; Moon, S.-J.; Löper, P.; Niesen, B.; Ledinsky, M.; Haug, F.-J.; Yum, J.-H.; Ballif, C. Organometallic Halide Perovskites: Sharp Optical Absorption Edge and Its Relation to Photovoltaic Performance. *J. Phys. Chem. C* **2014**, *5*, 1035−1139.

(3) Niu, S.; Huyan, H.; Liu, Y.; Yeung, M.; Ye, K.; Blankemeier, L.; Orvis, T.; Sarkar, D.; Singh, D. J.; Kapadia, R.; Ravichandran, J. Bandgap Control via Structural and Chemical Tuning of Transition Metal Perovskite Chalcogenides. *Adv. Mater.* **2017**, *29*, 1604733.

(4) Yusoff, A. R. b. M.; Kim, H. P.; Li, X.; Kim, J.; Jang, J.; Nazeeruddin, M. K. Ambipolar Triple Cation Perovskite Field Effect Transistors and Inverters. *Adv. Mater.* **2017**, *29*, 1602940.

(5) Chen, T.; Chen, W.-L.; Foley, B. J.; Lee, J.; Ruff, J. P. C.; Ko, J. Y. P.; Brown, C. M.; Harriger, L. W.; Zhang, D.; Park, C.; Yoon, M.; Chang, Y.-M.; Choi, J. J.; Lee, S.-H. Origin of long lifetime of band-edge charge carriers in organic-inorganic lead iodide perovskites. *Proc. Natl. Acad. Sci. U.S.A.* **2017**, *114*, 7519−7524.

(6) Jeon, N. J.; Noh, J. H.; Kim, Y. C.; Yang, W. S.; Ryu, S.; Seok, S. I. Solvent Engineering for High-performance Inorganic−organic Hybrid Perovskite Solar Cells. *Nat. Mater.* **2014**, *13*, 897.

(7) Back, H.; Kim, J.; Kim, G.; Kim, T. K.; Kang, H.; Kong, J.; Lee, S. H.; Lee, K. Interfacial Modification of Hole Transport Layers for Efficient Large-area Perovskite Solar Cells Achieved via Blade-coating. *Sol. Energy Mater. Sol. Cells* **2016**, *144*, 309−315.

(8) Ciro, J.; Mejía-Escobar, M. A.; Jaramillo, F. Slot-die Processing of Flexible Perovskite Solar Cells in Ambient Conditions. *Sol. Energy* **2017**, *150*, 570−576.

(9) Mathies, F.; Abzieher, T.; Hochstuhl, A.; Glaser, K.; Colsmann, A.; Paetzold, U. W.; Hernandez-Sosa, G.; Lemmer, U.; Quintilla, A. Multipass Inkjet Printed Planar Methylammonium Lead Iodide Perovskite Solar Cells. *J. Mater. Chem. A* **2016**, *4*, 19207−19213.

(10) Zhou, H.; Chen, Q.; Li, G.; Luo, S.; Song, T.-b.; Duan, H.-S.; Hong, Z.; You, J.; Liu, Y.; Yang, Y. Interface Engineering of Highly Efficient Perovskite Solar Cells. *Science* **2014**, *345*, 542−546.

(11) Xie, L.-Q.; Chen, L.; Nan, Z.-A.; Lin, H.-X.; Wang, T.; Zhan, D.-P.; Yan, J.-W.; Mao, B.-W.; Tian, Z.-Q. Understanding the Cubic Phase Stabilization and Crystallization Kinetics in Mixed Cations and Halides Perovskite Single Crystals. *J. Am. Chem. Soc.* **2017**, *139*, 3320−3323.

(12) Li, W.; Zhang, W.; Van Reenen, S.; Sutton, R. J.; Fan, J.; Haghighirad, A. A.; Johnston, M. B.; Wang, L.; Snaith, H. J. Enhanced UV-light Stability of Planar Heterojunction Perovskite Solar Cells with Caesium Bromide Interface Modification. *Energy Environ. Sci.* **2016**, *9*, 490−498.

(13) Wang, J. T.-W.; Wang, Z.; Pathak, S.; Zhang, W.; deQuilettes, D. W.; Wisnivesky-Rocca-Rivarola, F.; Huang, J.; Nayak, P. K.; Patel, J. B.; Mohd Yusof, H. A.; Vaynzof, Y.; Zhu, R.; Ramirez, I.; Zhang, J.; Ducati, C.; Grovenor, C.; Johnston, M. B.; Ginger, D. S.; Nicholas, R. J.; Snaith, H. J. Efficient Perovskite Solar Cells by Metal Ion Doping. *Energy Environ. Sci.* **2016**, *9*, 2892−2901.

(14) Saliba, M.; Matsui, T.; Domanski, K.; Seo, J.-Y.; Ummadisingu, A.; Zakeeruddin, S. M.; Correa-Baena, J.-P.; Tress, W. R.; Abate, A.; Hagfeldt, A.; Gratzel, M. Incorporation of Rubidium Cations into Perovskite Solar Cells Improves Photovoltaic Performance. *Science* **2016**, *354*, 206−209.

(15) Kaltenbrunner, M.; Adam, G.; Głowacki, E. D.; Drack, M.; Schwödiauer, R.; Leonat, L.; Apaydin, D. H.; Groiss, H.; Scharber, M. C.; White, M. S.; Sariciftci, N. S.; Bauer, S. Flexible high power-per-weight perovskite solar cells with chromium oxide-metal contacts for improved stability in air. *Nat. Mater.* **2015**, *14*, 1032−1039.

(16) Li, X.; Dar, M. I.; Yi, C.; Luo, J.; Tschumi, M.; Nazeeruddin, M. K.; Han, H.; Grätzel, M. Improved performance and stability of perovskite solar cells by crystal crosslinking with alkylphosphonic acid ω-ammonium chlorides. *Nat. Chem.* **2015**, *7*, 703−711.

(17) Xiong, H.; Rui, Y.; Li, Y.; Zhang, Q.; Wang, H. Hydrophobic coating over a CH3NH3PbI3 absorbing layer towards air stable perovskite solar cells. *J. Mater. Chem. C* **2016**, *4*, 6848−6854.

(18) Zhao, Y.; Wei, J.; Li, H.; Yan, Y.; Zhou, W.; Yu, D.; Zhao, Q. A Polymer Scaffold for Self-healing Perovskite Solar Cells. *Nat. Commun.* **2016**, *7*, 10228.

(19) Wang, F.; Geng, W.; Zhou, Y.; Fang, H.-H.; Tong, C.-J.; Loi, M. A.; Liu, L.-M.; Zhao, N. Phenylalkylamine Passivation of Organolead Halide Perovskites Enabling High-Efficiency and Air-Stable Photovoltaic Cells. *Adv. Mater.* **2016**, *28*, 9986−9992.

(20) Huang, Z.; Hu, X.; Liu, C.; Tan, L.; Chen, Y. Nucleation and Crystallization Control via Polyurethane to Enhance the Bendability of Perovskite Solar Cells with Excellent Device Performance. *Adv. Funct. Mater.* **2017**, *27*, 1703061.

(21) Manshor, N. A.; Wali, Q.; Wong, K. K.; Muzakir, S. K.; Fakharuddin, A.; Schmidt-Mende, L.; Jose, R. Humidity versus Photostability of Metal Halide Perovskite Films in a Polymer Matrix. *Phys. Chem. Chem. Phys.* **2016**, *18*, 21629−21639.

(22) Guo, Y.; Shoyama, K.; Sato, W.; Nakamura, E. Polymer Stabilization of Lead(II) Perovskite Cubic Nanocrystals for Semi-transparent Solar Cells. *Adv. Energy Mater.* **2016**, *6*, 1502317.

(23) Chaudhary, B.; Kulkarni, A.; Jena, A. K.; Ikegami, M.; Udagawa, Y.; Kunugita, H.; Ema, K.; Miyasaka, T. Poly(4-Vinylpyridine)-Based Interfacial Passivation to Enhance Voltage and Moisture Stability of Lead Halide Perovskite Solar Cells. *ChemSusChem* **2017**, *10*, 2473−2479.

(24) Di Giacomo, F.; Fakharuddin, A.; Jose, R.; Brown, T. M. Progress, Challenges and Perspectives in Flexible Perovskite Solar Cells. *Energy Environ. Sci.* **2016**, *9*, 3007−3035.

(25) Banerjee, A. N.; Maity, R.; Kundoo, S.; Chattopadhyay, K. K. Poole-Frenkel effect in nanocrystalline SnO2:F thin films prepared by a sol-gel dip-coating technique. *Phys. Status Solidi* **2004**, *201*, 983−989.

(26) Nie, W.; Tsai, H.; Asadpour, R.; Blancon, J.-C.; Neukirch, A. J.; Gupta, G.; Crochet, J. J.; Chhowalla, M.; Tretiak, S.; Alam, M. A.; Wang, H.-L.; Mohite, A. D. High-efficiency Solution-processed Perovskite Solar Cells with Millimeter-scale Grains. *Science* **2015**, *347*, 522−525.

(27) Frost, J. M.; Butler, K. T.; Brivio, F.; Hendon, C. H.; van Schilfgaarde, M.; Walsh, A. Atomistic Origins of High-Performance in Hybrid Halide Perovskite Solar Cells. *Nano Lett.* **2014**, *14*, 2584−2590.

(28) Perry, A. J.; Valvoda, V.; Rafaja, D. X-ray Residual Stress Measurement in TiN, ZrN and HfN Films Using the Seemann-Bohlin Method. *Thin Solid Films* **1992**, *214*, 169−174.

(29) Huang, J.; Yang, H.; Chen, M.; Ji, T.; Hou, Z.; Wu, M. An Infrared Spectroscopy Study of PES PVP Blend and PES-g-PVP Copolymer. *Polym. Test.* **2017**, *59*, 212−219.

(30) Liu, S.; Zeng, W.; Chen, T. Synthesis of Hierarchical Flower-like NiO and The Influence of Surfactant. *Phys. E* **2017**, *85*, 13−18.

(31) Gao, B.; Wu, Y. C.; Zhang, Z. G.; Hua, J. J.; Yao, K. D.; Hou, X. Poly(acrylamide-co-acrylic acid)/Poly(vinyl pyrrolidone) Polymer Blends Prepared by Dispersion Polymerization. *J. Macromol. Sci., Part B: Phys.* **2008**, *47*, 544−554.

(32) Tripathi, B.; Bhatt, P.; Kanth, P. C.; Yadav, P.; Desai, B.; Pandey, M. K.; Kumar, M. Temperature Induced Structural, Electrical and Optical Changes in Solution Processed Perovskite Material: Application in Photovoltaics. *Sol. Energy Mater. Sol. Cells* **2015**, *132*, 615−622.

(33) Qiu, J.; Qiu, Y.; Yan, K.; Zhong, M.; Mu, C.; Yan, H.; Yang, S. All-solid-state hybrid solar cells based on a new organometal halide perovskite sensitizer and one-dimensional TiO2 nanowire arrays. *Nanoscale* **2013**, *5*, 3245−3248.



DOI: 10.1021/acsami.8b04236
*ACS Appl. Mater. Interfaces* XXXX, XXX, XXX−XXX

(34) Lindblad, R.; Jena, N. K.; Philippe, B.; Oscarsson, J.; Bi, D.; Lindblad, A.; Mandal, S.; Pal, B.; Sarma, D. D.; Karis, O.; Siegbahn, H.; Johansson, E. M. J.; Odelius, M.; Rensmo, H. Electronic Structure of CH3NH3PbX3 Perovskites: Dependence on the Halide Moiety. *J. Phys. Chem. C* **2015**, *119*, 1818−1825.
(35) Dong, Q.; Shi, Y.; Zhang, C.; Wu, Y.; Wang, L. Energetically Favored Formation of $SnO_2$ Nanocrystals as Electron Transfer Layer in Perovskite Solar Cells with High Efficiency Exceeding 19%. *Nano Energy* **2017**, *40*, 336−344.
(36) Ryu, S.; Noh, J. H.; Jeon, N. J.; Kim, Y. C.; Yang, W. S.; Seo, J.; Seok, S. I. Voltage Output of Efficient Perovskite Solar Cells with High Open-circuit Voltage and Fill Factor. *Energy Environ. Sci.* **2014**, *7*, 2614−2618.
(37) Busacca, C.; Di Blasi, O.; Briguglio, N.; Ferraro, M.; Antonucci, V.; Di Blasi, A. Electrochemical performance investigation of electrospun urchin-like V 2 O 3 -CNF composite nanostructure for vanadium redox flow battery. *Electrochim. Acta* **2017**, *230*, 174−180.
(38) Kim, Y. C.; Jeon, N. J.; Noh, J. H.; Yang, W. S.; Seo, J.; Yun, J. S.; Ho-Baillie, A.; Huang, S.; Green, M. A.; Seidel, J.; Ahn, T. K.; Seok, S. I. Beneficial Effects of PbI2Incorporated in Organo-Lead Halide Perovskite Solar Cells. *Adv. Energy Mater.* **2016**, *6*, 1502104.
(39) Cho, K. T.; Paek, S.; Grancini, G.; Roldán-Carmona, C.; Gao, P.; Lee, Y.; Nazeeruddin, M. K. Highly Efficient Perovskite Solar Cells with a Compositionally Engineered Perovskite/Hole Transporting Material Interface. *Energy Environ. Sci.* **2017**, *10*, 621−627.
(40) Liu, Q.; Qin, M.-C.; Ke, W.-J.; Zheng, X.-L.; Chen, Z.; Qin, P.-L.; Xiong, L.-B.; Lei, H.-W.; Wan, J.-W.; Wen, J.; Yang, G.; Ma, J.-J.; Zhang, Z.-Y.; Fang, G.-J. Enhanced Stability of Perovskite Solar Cells with Low-Temperature Hydrothermally Grown SnO2Electron Transport Layers. *Adv. Funct. Mater.* **2016**, *26*, 6069−6075.
(41) Jiang, Q.; Zhang, L.; Wang, H.; Yang, X.; Meng, J.; Liu, H.; Yin, Z.; Wu, J.; Zhang, X.; You, J. Enhanced electron extraction using SnO2 for high-efficiency planar-structure HC(NH2)2PbI3-based perovskite solar cells. *Nat. Energy* **2016**, *2*, 16177.
(42) Alsari, M.; Pearson, A. J.; Wang, J. T.-W.; Wang, Z.; Montisci, A.; Greenham, N. C.; Snaith, H. J.; Lilliu, S.; Friend, R. Degradation Kinetics of Inverted Perovskite Solar Cells. *Sci. Rep.* **2018**, *8*, 5977.
(43) Im, J.-H.; Jang, I.-H.; Pellet, N.; Grätzel, M.; Park, N.-G. Growth of CH3NH3PbI3 cuboids with controlled size for high-efficiency perovskite solar cells. *Nat. Nanotechnol.* **2014**, *9*, 927−932.
(44) Wu, X.; Trinh, M. T.; Niesner, D.; Zhu, H.; Norman, Z.; Owen, J. S.; Yaffe, O.; Kudisch, B. J.; Zhu, X.-Y. Trap States in Lead Iodide Perovskites. *J. Am. Chem. Soc.* **2015**, *137*, 2089−2096.
(45) Fakharuddin, A.; Di Giacomo, F.; Palma, A. L.; Matteocci, F.; Ahmed, I.; Razza, S.; D'Epifanio, A.; Licoccia, S.; Ismail, J.; Di Carlo, A.; Brown, T. M.; Jose, R. Vertical TiO2 Nanorods as a Medium for Stable and High-Efficiency Perovskite Solar Modules. *ACS Nano* **2015**, *9*, 8420−8429.
(46) Ryu, U.; Jee, S.; Park, J.-S.; Han, I. K.; Lee, J. H.; Park, M.; Choi, K. M. Nanocrystalline Titanium Metal-Organic Frameworks for Highly Efficient and Flexible Perovskite Solar Cells. *ACS Nano* **2018**, *12*, 4968−4975.


DOI: 10.1021/acsami.8b04236
*ACS Appl. Mater. Interfaces* XXXX, XXX, XXX−XXX